Design and Development of Lightly Alloyed Ferritic Fire-Resistant Structural Steels

CAMERON T. GROSS, DIETER ISHEIM, SEMYON VAYNMAN, MORRIS E. FINE, and YIP-WAH CHUNG

To improve safety in case of building fires, stricter building codes have been proposed requiring structural steels to maintain two-thirds of their room-temperature yield strength after exposure to 873 K (600 °C) for longer than 20 minutes. To address this need, we have designed lightly alloyed structural steels, employing computational thermodynamics in combination with fundamental principles of precipitation strengthening and its temperature dependence, precipitate stability, characterization by optical microscopy and atom probe tomography (APT), and mechanical testing at room and elevated temperatures. The design process resulted in low-carbon ferritic steels with small alloying additions of V, Nb, and Mo that maintain over 80 pct of room-temperature yield strength in compression, and nearly 70 pct in tension, after 2 hours of exposure at 873 K (600 °C). APT demonstrates the formation of nanoscale MX and M_2X (where M = V + Nb + Mo and X = C + N) precipitates after exposure to 873 K (600 °C). The favorable high-temperature mechanical properties are discussed with a model of precipitation strengthening by detachment-stress-mediated dislocation pinning at nanoscale semi-coherent MX precipitates.

https://doi.org/10.1007/s11661-018-4985-5

I. INTRODUCTION

STRUCTURAL steels used in construction today weaken markedly when heated above room temperature, typically losing more than half of their room-temperature yield strength in the temperature range approaching 873 K (600 °C).[1–3] Depending on the fuel source of a building fire, structural components can reach temperatures from 873 K (600 °C) to over 1273 K (1000 °C).[1,4] Rigid board insulation, intumescent paints, and spray coatings are used to slow the temperature rise within the structure and extend the time of structural safety.[5] Application of these materials adds about 50 pct to the total cost of the steel.[6] Current US building codes require structural steels to maintain 50 pct of their room-temperature yield strength when heated to 811 K (538 °C).[3]

The American Society for Testing and Materials (ASTM) and the National Institute of Standards and Technology (NIST) are considering the adoption of stricter building codes in which structural steels for buildings must maintain two-thirds of the room-temperature yield strength when exposed to 866 K (593 °C).[5,6] The goal of this research is to design and develop alloys that meet or exceed this proposed standard using low concentrations (< 0.4 wt pct total) of principal alloying elements (Mo + V + Nb) and maintaining excellent weldability through low carbon content. Increasing the high-temperature yield strength will increase the time to failure of important structural elements in case of a building fire, while low concentrations of alloying elements make the alloy cost-competitive with existing options. Several fire-resistant steel prototypes have been developed previously to meet the proposed standard, some requiring proprietary thermo-mechanical treatments.[2,7–10] The content of principal alloying elements (Mo + V + Nb) in these prototype alloys ranges from 0.5 wt pct[7,8,10] to about 1 wt pct.[2,9] Some of these prototypes require water quenching and have a higher carbon content (0.1 wt pct or more),[11] which may impact weldability. Other steel prototypes contain alloying elements similar to ours, but require a controlled cooling step; compositions of these prototypes appear to be derived from intuition rather than rational materials design principles.[12]

CAMERON T. GROSS, SEMYON VAYNMAN, MORRIS E. FINE, and YIP-WAH CHUNG are with the Department of Materials Science and Engineering, Northwestern University, 2220 Campus Drive, Evanston, IL 60208. DIETER ISHEIM is with the Department of Materials Science and Engineering, Northwestern University and also with Northwestern University Center for Atom Probe Tomography (NUCAPT), 2220 Campus Drive, Evanston, IL 60208. Contact e-mail: isheim@northwestern.edu

Manuscript submitted January 2, 2018.
Article published online October 30, 2018

There are two temperature regimes of interest when considering the strength of a typical structural steel, depending on the mechanism of slip or dislocation glide activation for plastic deformation: a "room-temperature," or athermal, regime and a high-temperature, or thermal, regime.[2,10] The athermal regime is associated with dislocation pinning by obstacles such as second-phase precipitates, dislocation forests, or grain boundaries. In this athermal regime, the decrease in yield strength with increasing temperature is gradual, while the thermal regime shows a rapid decrease in yield strength caused by thermally activated processes. These processes include atomic diffusion, Ostwald ripening (coarsening) of precipitates, thermal activation of dislocation climb, and dislocation recovery and annihilation.

In the present work, the design process is based on forming a network of mono-carbonitride (MX, where M = Nb, V, and X = C, N) precipitates as obstacles for dislocation motion, delaying the onset of the thermal regime to higher temperatures, and slowing the decrease of yield strength within the thermal regime. The precipitating carbide phases are selected so that precipitate formation can progress *in situ* in the temperature range targeted for fire resistance, in analogy to secondary-hardening precipitation strengthening during a dedicated heat treatment. We use computational thermodynamics to guide the design process, exploring a large compositional and temperature parameter space without the need of repeated prototyping of alloys. Additional design principles are outlined in the following.

Interfacial coherency between the MX precipitate and the matrix affects dislocation pinning and thus the strengthening contribution, but also the rates of nucleation, growth, and coarsening at elevated temperatures. Under quasi-static testing conditions, Arzt and coworkers suggested[13–16] that there exists an attractive interaction between the dislocation and the incoherent or semi-coherent precipitate interface, generating a positive detachment stress that must be overcome by thermal activation for the dislocation to glide, if the obstacle cannot be bypassed by dislocation bowing (Orowan process). The detachment stress increases with increasing interaction between dislocation and precipitate, for instance an elastic interaction due to the lattice mismatch between the precipitate and the matrix. A higher detachment stress will serve to slow the loss of strength with higher temperatures. At the same time, we must maintain a fine dispersion of precipitates to maximize the contribution from Orowan strengthening. It is thus necessary to minimize the coarsening rate of these precipitates at elevated temperatures. The basic principles of coarsening are captured by the Lifshitz–Slyozov–Wagner model,[17,18] which establishes that the rate of increase of the precipitate mean radius $\langle R \rangle$ is related to the interfacial free energy (γ) as follows:

$$\langle R \rangle^3 - \langle R_0 \rangle^3 = \kappa t, \qquad [1]$$

where κ is the coarsening coefficient, given by

$$\kappa = \frac{8\gamma c_\infty v_m^2 D}{9RT} \qquad [2]$$

with $\langle R_0 \rangle$ the mean radius at the beginning of the coarsening experiment, c_∞ the equilibrium solubility of the solute in the matrix, v_m the molar volume, D the diffusion coefficient, R the ideal gas constant, T the absolute temperature, and t the aging time. Slow coarsening or a small coarsening coefficient, κ, requires the precipitates to contain at least one component with low matrix solubility and small diffusion coefficient to establish a rate-limiting step. For alloys presented in this paper, V and specifically Nb will be the constituents chosen with small diffusion coefficients in the bcc Fe matrix. Matrix solubility relative to and in equilibrium with the mono-carbide MX phase is evaluated by thermodynamic modeling for rapid screening of the compositional parameter space, and verified by measuring the local composition in matrix and precipitates by atom probe tomography.

The interfacial energy γ depends on the degree of coherency of the interface between the precipitate and the matrix. Smaller γ, as would occur in coherent interfaces, results in slower coarsening. Small MX-type precipitates with a B1-type rock-salt structure have a semi-coherent interface in ferritic steels.[19] For the fire-resistant steels discussed here, carbide precipitates consist primarily of VC[20] and NbC.[21] These precipitates form with a Baker–Nutting relationship: $(100)_{\alpha\text{-Fe}} || (100)_{MX}$ and $[010]_{\alpha\text{-Fe}} || [110]_{MX}$.[22,23] At room temperature, bcc iron has a lattice parameter of 0.287 nm, and VC and NbC have lattice parameters of 0.417 nm[24] and 0.447 nm,[25,26] respectively. The lattice mismatch δ between the carbide and the ferrite matrix along the $[100]_{\alpha\text{-Fe}}$ and $[010]_{\alpha\text{-Fe}}$ direction, defined as $\delta = \{a_{[100]MX} - \sqrt{2}a_{[100]\alpha\text{-Fe}}\}/\sqrt{2}a_{[100]\alpha\text{-Fe}}$, is 2.8 pct for VC and 10.2 pct for NbC and thus depends on the precipitate composition. Specifically, the critical radius for the loss of coherency depends on the V content, as reported by Miyata *et al.*[27] Naturally, the nominal stoichiometry and exact crystallographic structure of very small precipitates in the nanometer range, as presented in the following, is an assumption, and is very difficult to observe experimentally, given the small size of the precipitates.

To achieve the proposed high-temperature yield strength ratio of two-thirds, we will use semi-coherent MX carbonitride precipitates in order to attain "best of both worlds" compromise: the precipitate–matrix lattice mismatch should be large enough to sustain a significant detachment stress and small enough to achieve slow coarsening. Precipitation of a fine dispersion of particles that are resistant to coarsening should increase the high-temperature yield strength ratio of the steels. Equilibrium thermodynamic modeling will be used to guide the design process, reducing the number of compositions that must be experimentally investigated.

II. EXPERIMENTAL METHODS

A. *Thermodynamic Modeling*

Equilibrium thermodynamic modeling was conducted using the Thermo-Calc software package. Calculations were conducted using idealized alloys with no

impurities, specifically nitrogen. This was done in order to simplify calculations and reduce the need for suspending extraneous phases. Since small amounts of nitrogen are easily introduced in practical steel production, the results from thermodynamic modeling thus need to be understood as the limiting case of very low nitrogen concentration. The database used was the SGTE Solutions Database version 2.1 (SSOL2), which was developed by the Scientific Group Thermodata Europe.

B. *Atom Probe Tomography*

Atom probe tomography (APT) was used to study the formation and evolution of precipitates of prototype alloys as a function of high-temperature exposure. Samples were machined to 300 μm × 300 μm × 12.7 mm rectangular blanks. Each sample was then electropolished to a sharp tip using two different electrolytes: a solution of 10 pct perchloric acid in acetic acid for neck formation and 2 pct perchloric acid in butoxyethanol for final polishing. Field-evaporation was conducted using voltage ramped from 0 V to approximately 7 kV. Field-evaporation was thermally activated by 20 pJ UV (355 nm wavelength) laser pulses at 500 kHz repetition rate. Data analysis was conducted using the Integrated Visualization and Analysis Software (IVAS) software suite developed by CAMECA.[28]

The volume-equivalent radii of precipitates were calculated as follows: (i) the detection efficiency of the atom probe (50 pct) was applied to determine the actual number of metal (Nb + V + Mo) atoms in the precipitate; (ii) the precipitate volume v was determined by calculating the number of unit cells from the number of metal atoms and using the composition-weighted average of NbC (a_{NbC} = 0.447 nm[25,26]) and VC (a_{VC} = 0.417 nm[24]); and (iii) the volume was equated to that of a sphere with a volume-equivalent radius r_v, as shown below:

$$V = \frac{N_{metal}\Omega}{fm}\left(x_{Nb}a_{NbC} + x_{V}a_{VC}\right)^3, \quad [3]$$

$$r_V = \left(\tfrac{3}{4\pi}V\right)^{1/3}, \quad [4]$$

where N_{metal} is the number of metal atoms detected from the carbide precipitate in the APT reconstruction, f the detection efficiency (f = 0.5 for the LEAP4000X Si atom probe tomograph used here), Ω the volume of the unit cell, m the number of metal atoms in the unit cell (m = 4 for the fcc-type representation of the unit cell of the B2 structure used here), and x_{Nb} and x_V the atomic fractions of Nb and V, respectively, and a_{NbC} and a_{VC} are the lattice parameters of NbC and VC, respectively.

C. *Mechanical Testing*

All mechanical tests were conducted in accordance with ASTM standards E209-00, E21-09, and E9-89a.[29–31] In tensile testing, specimens had a testing segment with a cross section of 6.35 mm in diameter by 31.75 mm in length. Tensile testing was conducted using a screw-driven frame. High-temperature tensile tests were conducted in a cylindrical furnace under atmospheric conditions. A 25.4-mm extensometer was used to measure strain during tensile testing. Compression testing was conducted using a hydraulically driven load frame. Compression specimens measured 6.35 mm in diameter by 19 mm tall for a 3:1 aspect ratio. Strain was calculated from machine compliance and crosshead displacement. All tests were conducted at the ASTM standard strain rate of 0.005 ± 0.002 1/min. For high-temperature testing, the sample temperature was ramped from room temperature to 873 K (600 °C) at a rate of approximately 7 K min^{-1} as verified by a thermocouple in contact with the sample. This temperature was maintained for either 20 minutes or 2 hours prior to testing, depending on the desired test length. Yield strengths were measured at 0.2 pct strain offset.

III. RESULTS AND DISCUSSION

A. *Thermodynamic Modeling*

Compositions were chosen for the Thermo-Calc-modeled alloys containing C, Cr, Mo, V, Nb, and Fe (balance) as shown in Table I. This was done to create a simple model to investigate compositions of interest without including effects due to impurity elements. The Nb concentration was set at 0.07 wt pct. A fractional factorial design was used to reduce the number of compositions while still spanning the parameter space of interest.

Figure 1 shows isopleths of several selected compositions *vs* vanadium content. For simplicity, only ferrite, austenite, cementite, MX, and M_2X phases were included in the calculation. Higher-order carbides ($M_{23}C_6$, *etc.*) were ignored due to the low Cr and C content impeding their formation.[32]

Our goal is to choose alloy compositions to maximize the ferrite + MX phase field to ensure thermodynamic stability of the MX phase in a wide range of compositions and temperatures. From these isopleths, one can see that the ferrite + MX phase field is most prominently observed with carbon content at or below 0.08 wt pct and vanadium content greater than 0.15 wt pct. Chromium appears to be detrimental to MX stability at high temperatures due to expanding the stability range of the cementite phase to higher

Table I. Compositions (in Wt Pct) of the Alloys Evaluated with Thermodynamic Modeling (Balance Fe)

Alloys	C	Cr	Mo	V	Nb
1	0.08	0.25	0.01	0.05	0.07
2	0.05	0.50	0.01	0.05	0.07
3	0.05	0.25	0.15	0.05	0.07
4	0.05	0.25	0.01	0.2	0.07
5	0.05	0.50	0.15	0.2	0.07
6	0.08	0.25	0.15	0.2	0.07
7	0.08	0.50	0.01	0.2	0.07
8	0.08	0.50	0.15	0.05	0.07

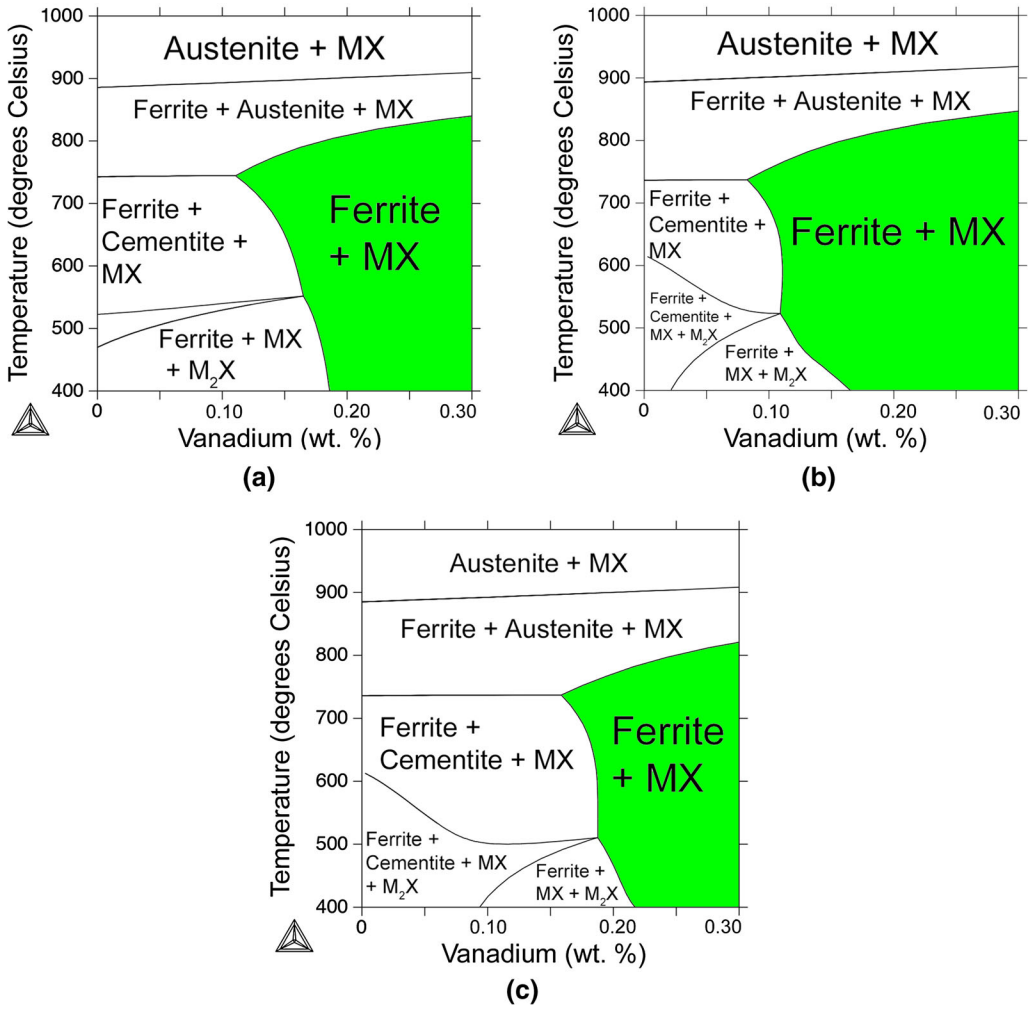

Fig. 1—Vanadium isopleths calculated using Thermo-Calc for the following compositions in wt pct: (*a*) 0.05C-0.25Cr-0.15Mo-0.07Nb, (*b*) 0.08C-0.25Cr-0.15Mo-0.07Nb, and (*c*) 0.05C-0.5Cr-0.01Mo-0.07Nb.

vanadium concentrations, as shown in Figure 1(c). One may conclude that in order to precipitate a high volume fraction of the MX phase at 873 K (600 °C) without competition from other carbide phases, the alloy should have V content greater than 0.15 wt pct and carbon content less than 0.1 wt pct. We observed a correlation between predicted MX phase fraction and high-temperature yield strength, as presented later. Nitrogen impurities, which are not considered in our thermodynamic modeling, would further stabilize the MX phase and further increase the MX phase fraction. The extent of the MX phase field thus represents a lower bound, relative to the presence of small amounts of nitrogen.

Table II. Measured Compositions of Experimental Fire-Resistant Structural Steel (FRSS) Alloys

Alloys	C	Cr	Mo	V	Nb	Mn	Si
FRSS-3							
Wt Pct	0.042	0.234	0.143	0.019	0.07	1.408	0.204
At. Pct	0.195	0.251	0.083	0.021	0.042	1.427	0.404
FRSS-5							
Wt Pct	0.07	0.22	0.13	0.18	0.06	1.23	0.19
At. Pct	0.324	0.235	0.075	0.197	0.036	1.245	0.376
FRSS-6							
Wt Pct	0.032	—	0.13	0.19	0.07	1.21	0.23
At. Pct	0.148	—	0.075	0.208	0.042	1.226	0.456

B. *Alloy Composition and Optical Metallography*

The three experimental alloys studied in this work are designated fire-resistant structural steel (FRSS)-3, -5, and -6. FRSS-3 is a commercial alloy provided by Nucor. FRSS-5 and -6 were fabricated by Sophisticated Alloys according to our specifications. Table II gives the composition of the three experimental alloys. All alloys were normalized at 1323 K (1050 °C) for 1 hour and air-cooled. Compositions of FRSS-3 and -5 are similar to the idealized alloys -3 and -6, respectively, while the composition of FRSS-6 is similar to that of FRSS-5, except for lower C content and the absence of Cr, as shown in Table II.

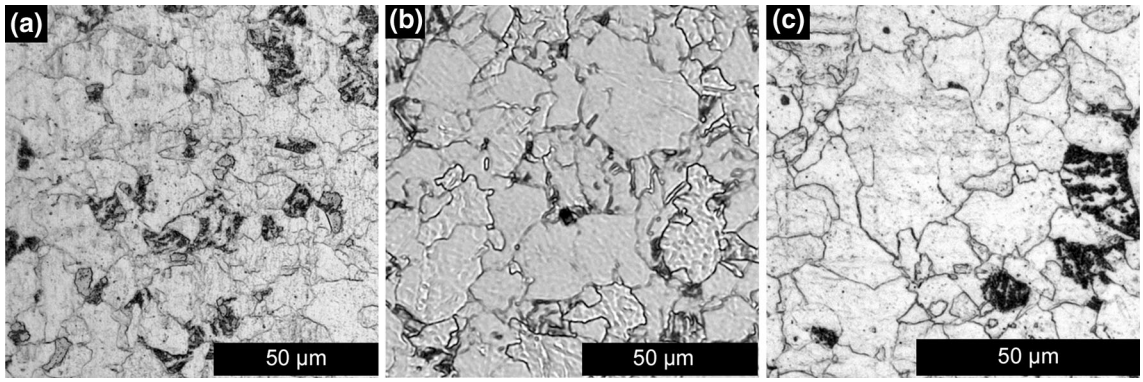

Fig. 2—Optical micrographs of (*a*) FRSS-3, (*b*) FRSS-5, and (*c*) FRSS-6. All samples were normalized at 1323 K (1050 °C) for 1 h and air-cooled. Samples were etched with a 2 pct Nital solution.

Figure 2 shows optical micrographs of these three alloys after normalization and air-cooling. One can observe primarily large ferrite grains with a mixture of pearlite and bainite.

C. *Atom Probe Tomography*

Figure 3 shows APT reconstructions of FRSS-3 after 0, 2, and 6 hours of exposure to 873 K (600 °C) followed by water quench. In each image, only C (black) and Nb (purple) atoms are shown for clarity. APT reveals the formation of metal carbonitride clusters with diameter 1 nm or smaller after 2 hours of exposure to 873 K (600 °C) (Figure 3(b)). Formation of distinct precipitates becomes apparent after 6 hours of exposure to 873 K (600 °C). In Figure 3(c), isoconcentration surfaces of 1 at. pct C and 1 at. pct Nb are shown to highlight the precipitates. APT reconstructions show evidence of carbide precipitation with increasing time at 873 K (600 °C).

Figures 3(d) and (e) show radial concentration profiles for select MX and M_2X precipitates after 6 hours of exposure to 873 K (600 °C) in FRSS-3. A higher concentration of nitrogen is observed at the center of the precipitates. This may be due to the precipitate nucleating on a NbN or VN core that grows and evolves in composition as N and C diffuse through the ferrite at high temperatures.[20] The average diameter of these precipitates is about 2 nm after 6-hour exposure to 873 K (600 °C).

Figure 4(a) compares the elemental composition of MX precipitates predicted by Thermo-Calc with the average composition obtained from MX precipitates in FRSS-3 after 6-hour exposure to 873 K (600 °C). For Mo, V, and Nb, the values observed by APT are near the predicted values, showing that MX precipitates achieve near-equilibrium composition after 6 hours of exposure to 873 K (600 °C).

Figure 4(b) shows the (C + N)/(Mo + V + Nb) ratio *vs* volume-equivalent radius (r_v) of precipitates and (c) the corresponding histogram distribution obtained from FRSS-3 exposed to 873 K (600 °C) for 6 hours. Compositions are calculated without Fe. N atoms substitute for carbon in the MX precipitates.[20] The (C + N)/(Mo + V + Nb) ratio varies between approximately 0.4 and 1.0, compatible with the presence of both M_2X and MX-type carbide precipitates. The precipitate radii fall between 0.5 and 1.2 nm, corresponding to precipitates of 120 to 400 atoms. At this precipitate size, a clear experimental distinction between M_2X and MX-type carbide precipitates is extremely difficult and goes beyond the scope of the present study. The precipitate radii are, however, within the realm of coherency for MX precipitates (1.6 to 2.5 nm).[27]

Figures 5(a) through (c) show atom probe reconstructions for FRSS-6 as-cooled, after 8, and 27 hours at 873 K (600 °C), respectively. We see that the precipitate size remains small after 27 hours of aging at 873 K (600 °C), with a mean radius of 1.01 ± 0.14 nm. These precipitates demonstrate excellent coarsening resistance at 873 K (600 °C). Figure 5(d) shows radial concentration profiles for a typical MC precipitate after 27 hours of aging at 873 K (600 °C). No nitrogen was detected by APT in the MX-type carbide precipitates of this alloy.

Figure 6(a) compares the composition of the carbide precipitates in FRSS-6 after 27-hour exposure to 873 K (600 °C) measured by APT *vs* the equilibrium composition as predicted by Thermo-Calc. The measured vanadium concentration is higher, and Mo and Nb concentration lower than the predicted values. This may be due to the higher V concentration in FRSS-6, compared to FRSS-3, and different diffusion coefficients between V, Nb, and Mo, resulting in FRSS-6 precipitates not yet reaching their equilibrium composition.

Figure 6(b) shows the C/(Mo + V + Nb) ratio *vs* volume-equivalent radius (r_v) of precipitates and (c) the corresponding histogram distribution obtained from FRSS-6 exposed to 873 K (600 °C) for 27 hours, with the measured C/(Mo + V + Nb) ratio varying between 0.3 and 0.75. Since the carbon concentration can be underestimated in APT, it can be extremely difficult to discriminate between M_2X and MX phases based on the measured metal-to-carbon ratio, specifically for very small nm-sized precipitates as observed here. The volume-equivalent radii of the precipitates in FRSS-6 fall between 0.8 and 1.25 nm, roughly the same size as

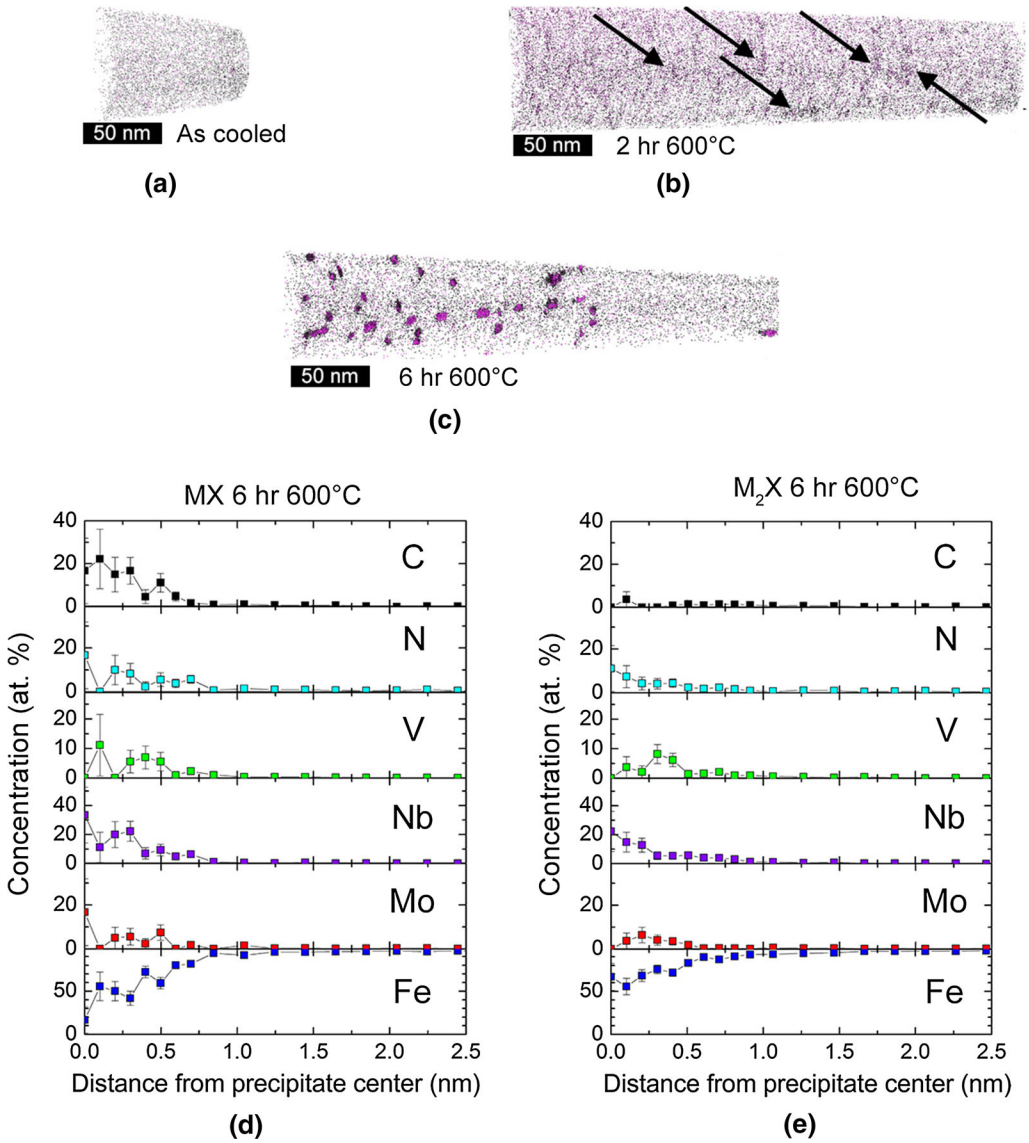

Fig. 3—Atom probe tomography reconstructions of normalized FRSS-3: (*a*) air-cooled, (*b*) after 2 h of aging, and (*c*) after 6 h of aging at 873 K (600 °C). Only Nb (purple) and C (black) atoms are shown for clarity. Arrows in (b) highlight select carbide precipitates. In (c), 1 at. pct Nb and 1 at. pct C isoconcentration surfaces have been superposed to highlight precipitates. Radial concentration profiles for representative MX (*d*) and M_2X precipitates (*e*) in FRSS-3 after 6-h exposure to 873 K (600 °C). Elements shown are Nb (purple), N (cyan), Mo (red), V (green), C (black), and Fe (blue) (Color figure online).

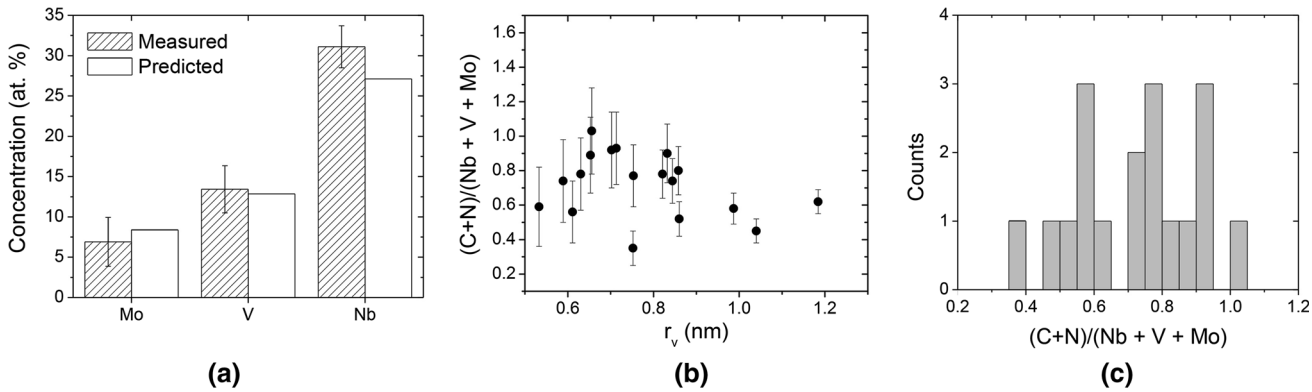

Fig. 4—(*a*) Average elemental composition of MX precipitates in FRSS-3 after 6-h exposure to 873 K (600 °C) measured by APT *vs* equilibrium composition predicted by Thermo-Calc, (*b*) (C + N)-to-metal ratio *vs* volume-equivalent radius of precipitates in FRSS-3 after 6-h exposure to 873 K (600 °C). (*c*) Histogram of precipitate (C + N)-to-metal ratio distribution.

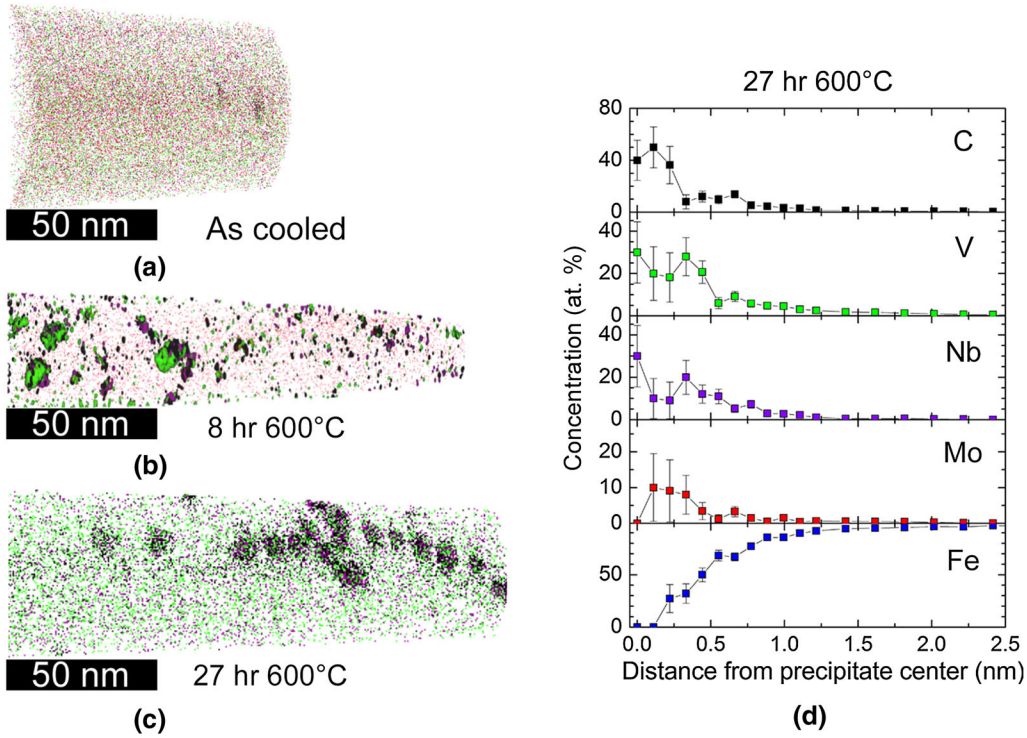

Fig. 5—Atom probe tomography reconstructions of FRSS-6. For clarity, only C (black), V (green), Nb (purple), and Mo (red) atoms are shown. (*a*) As-cooled, (*b*) after 8 h, and (*c*) after 27 h at 873 K (600 °C). 1 at. pct V, Nb, and C isoconcentration surfaces (green, purple, and black, respectively) are superposed in (b) to highlight the carbide precipitates. An APT radial concentration profile of a typical precipitate after 27 h of aging at 873 K (600 °C) is shown in (*d*). No nitrogen was detected by APT (Color figure online).

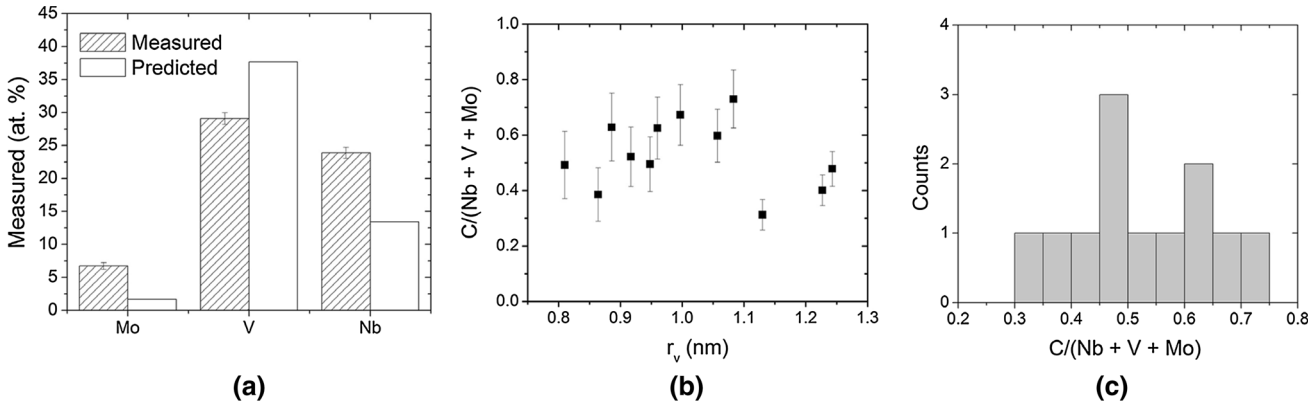

Fig. 6—(*a*) Average elemental composition of precipitates in FRSS-6 after 27-h exposure to 873 K (600 °C) measured by APT *vs* equilibrium composition predicted by Thermo-Calc, (*b*) carbon-to-metal ratio *vs* volume-equivalent radius of precipitates, and (*c*) histogram representation of the carbon-to-metal ratio distribution, in FRSS-6 after 27-h exposure to 873 K (600 °C).

the precipitates observed in FRSS-3, despite being aged for over three times as long. The observed thermal stability of the precipitates, together with the thermodynamic calculations do, however, indicate that MX is the preferred carbide phase in FRSS-6.

D. *Mechanical Testing*

Figure 7 shows typical compressive stress–strain curves for FRSS-3 and -6 at room temperature and at 873 K (600 °C). Figure 7(c) shows the variation of compressive yield strength of FRSS-6 as a function of time at 873 K (600 °C).

The ratio of high-temperature to room-temperature yield strength for FRSS-6 is over 80 pct, compared to 64 pct for FRSS-3. The compressive yield strength of FRSS-6 was maintained constant even after 2 hours of hold time at 873 K (600 °C). This strength retention correlates well with the observed slow coarsening rate of MX precipitates.

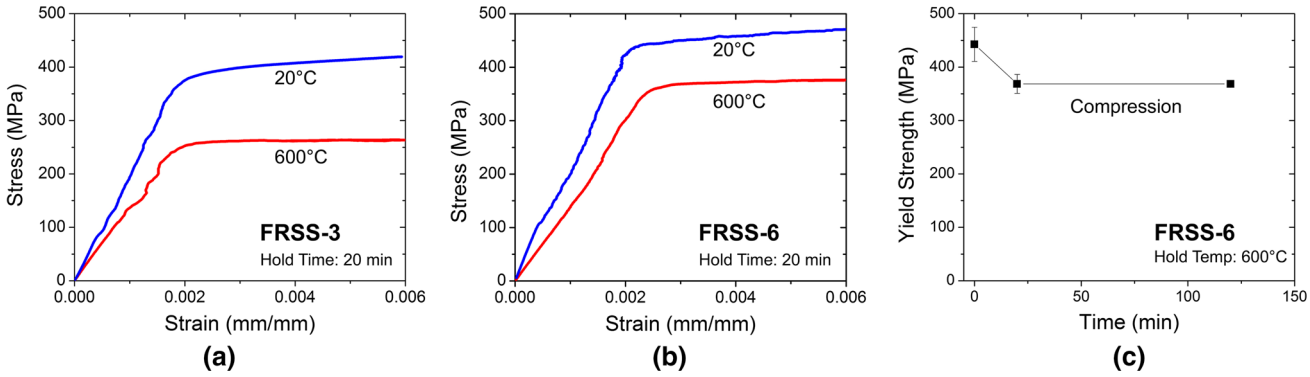

Fig. 7—Engineering stress–strain curves for compression of (*a*) FRSS-3 and (*b*) FRSS-6 at room temperature (blue) and at 873 K (600 °C) (red) after 20 min of exposure. (*c*) Compressive yield strength for FRSS-6 at 873 K (600 °C) *vs* hold time (Color figure online).

Table III. Yield Strength at 873 K (600 °C) ($\sigma_{y,600}$), at Room Temperature ($\sigma_{y,RT}$), and Yield Strength Ratio $\sigma_{y,600}/\sigma_{y,RT}$ for Three Ferritic Alloys Under Compression and Tension

Alloys	Testing Modes	$\sigma_{y,600}$ (MPa)	$\sigma_{y,RT}$ (MPa)	$\sigma_{y,600}/\sigma_{y,RT}$
FRSS-3	Compression	264 ± 15	401 ± 3	0.64 ± 0.03
	Tension	232 ± 19	346 ± 8	0.67 ± 0.06
FRSS-5	Compression	348 ± 16	485 ± 17	0.72 ± 0.04
	Tension	*	*	*
FRSS-6	Compression	368 ± 18[†]	442 ± 32	0.83 ± 0.07
	Tension	284 ± 33[†]	409 ± 40	0.69 ± 0.10

*FRSS-5 tension data omitted due to lack of sufficient materials.
[†]873 K (600 °C) FRSS-6 test results reported after 2-h hold time.

Table III summarizes the yield strength data for all three experimental alloys, showing the yield strength at 873 K (600 °C) ($\sigma_{y,600}$) and at room temperature ($\sigma_{y,RT}$), the yield strength ratio $\sigma_{y,600}/\sigma_{y,RT}$, as well as the calculated MX phase fraction for each alloy. We see that alloys FRSS-5 and -6 perform very well, exceeding the two-thirds yield strength ratio at 873 K (600 °C).

The composition of FRSS-5 and -6 differs from that of FRSS-3 in one major aspect: a substantial increase of V concentration, which results in a marked increase of MX phase fraction and elimination of M_2X phase, as indicated by thermodynamic modeling. Thermo-Calc shows that FRSS-5 and -6 contain approximately 0.62 and 0.35 mol pct MX, respectively, and no M_2X at 873 K (600 °C), compared with 0.15 MX and 0.29 pct M_2X for FRSS-3. Both FRSS-5 and -6 achieve compressive yield strength ratio greater than 0.7, compared with 0.64 for FRSS-3, suggesting that the MX mol pct is a factor in increased high-temperature strength, due to the slow coarsening of MX precipitates. In addition to the overall mole percent, the composition of the MX phase may also play a role in the high-temperature yield strength of these alloys. As shown in Figures 4(a) and 6(a), FRSS-6 has a higher V content in the precipitates when compared to FRSS-3. The composition of the MX phase will influence the interfacial strain energy, which may also play a part in high-temperature yield strength. Figure 8 shows the temperature dependence of compression and tension yield strength for FRSS-6. FRSS-6 satisfies the target yield strength ratio of two-thirds at 873 K (600 °C) in tension, and 898 K (625 °C) in compression.

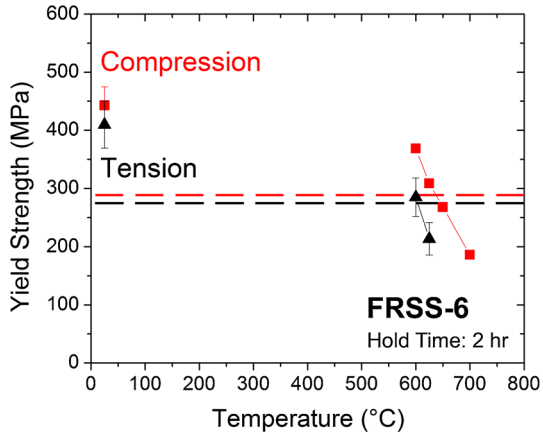

Fig. 8—Compressive (red squares) and tensile (black triangles) yield strength *vs* temperature for FRSS-6. Tests were conducted after a 2-hour hold time at the respective elevated temperatures. Dashed lines indicate two-thirds of room-temperature yield strength ($\sigma_{y,600}/\sigma_{y,RT}$) for compression (red) and tension (black), respectively (Color figure online).

Table IV. Lattice Parameter Values a and Calculated Lattice Misfit δ for VC, NbC, and Mixed-Composition Precipitates Based on the Compositions Measured by Atom Probe Tomography, in FRSS-3 and -6

	VC	NbC	FRSS-3	FRSS-6
a (nm) at 298 K	0.417*	0.447**	0.438	0.431
δ at 298 K	0.028	0.102	0.083	0.066
a (nm) at 873 K	0.419*	0.448**	0.439	0.432
δ at 873 K	0.025	0.096	0.074	0.055

*From Ref. [24].
**From Ref. [26].

E. *Detachment Stress Analysis*

We now discuss the significance of detachment stress resulting from an attractive interaction between gliding dislocations and nanoscale precipitates following the approach first proposed by Arzt and coworkers.[13–16] The detachment stress is evaluated with the dislocation in a position at the back side of a precipitate relative to the glide direction, that is the dislocation may have already cut through or climbed over the precipitate to its back side, with the detachment stress being the only interaction that prevents the dislocation from breaking free from the precipitate. For reference and for scaling, we will use the Orowan stress τ_o as the maximum possible strength that can be achieved by the given dispersion of small precipitates that act as "hard" obstacles, *i.e.*, the dislocations are unable to penetrate or free themselves from these precipitates except by looping around *via* the Orowan mechanism.

We begin our analysis with a simple elastic model that incorporates the misfit at the matrix–precipitate interface and the precipitate size as controlling factors of the dislocation stress. For simplicity, we consider only MX-type carbide precipitates. As discussed in the introduction section, the linear lattice mismatch δ between the bcc Fe matrix and MX precipitate in the (001) plane is approximately 2.8 pct for VC and 10.2 pct for NbC at room temperature, and somewhat smaller, 2.5 pct and 9.6 pct at 873 K (600 °C), respectively. Table IV lists the lattice parameters and maximum misfits at 298 K and 873 K (20 °C and 600 °C) between the bcc Fe matrix and VC, NbC, and mixed-composition precipitates with the compositions measured by APT in FRSS-3 and -6. The lattice parameter for bcc Fe is 0.289 nm at 873 K (600 °C). Increasing the vanadium concentration in the MC precipitate lowers the misfit between the precipitate and the iron matrix (Table IV).

The interfacial strain energy can be estimated using the energy of the strained two-dimensional interface multiplied by a characteristic length:

$$E_{\text{strain}} = \frac{1}{2} Y \delta^2 r, \qquad [5]$$

where Y is Young's modulus of the matrix, δ the misfit parameter, and r the particle radius.

Following the approach developed by Arzt and Rösler,[15] we model the attractive interaction between a dislocation line and a particle (synonymous with "precipitate" in this case) as

$$T_P = kT_M, \qquad [6]$$

where T_P is the line energy of a dislocation in contact with the particle, k the so-called relaxation factor ($0 \le k \le 1$) where $k = 1$ means no relaxation and no detachment stress, and T_M is the line energy of a free dislocation in the matrix far from the particle. We can approximate $T_M \cong \frac{1}{2} Gb^2$, where G is the shear modulus and b is the Burgers vector, so $T_M = 1.97 \times 10^{-9}$ J m^{-1} in bcc iron at room temperature. We use the shear modulus of Fe $G = 79$ GPa at room temperature and $G = 51$ GPa at 873 K (600 °C), as we measured a roughly 35 pct reduction in Young's modulus from the elastic part of the stress/strain curves in Figure 7, and we assume the shear modulus will follow a similar temperature dependence. At 873 K (600 °C), we assume that a line dislocation makes contact with half of the particle circumference as it moves past the particle and the relaxation can be expressed as

$$T_{\text{relax}} = \pi r E_{\text{strain}}. \qquad [7]$$

Therefore, the total line tension of the dislocation in contact with the particle is given by

$$T_P = T_M - T_{\text{relax}} \qquad [8]$$

and k is given by

$$k = \frac{T_P}{T_M} = \frac{T_M - T_{\text{relax}}}{T_M}. \qquad [9]$$

At high temperatures, a correction factor is used[15] to reflect that thermal activation can help the dislocation to overcome the detachment stress, effectively reducing the barrier:

$$k_{\text{adjusted}} = k + \frac{k_B T}{Gb^2 r} \ln\left(\frac{\dot{\varepsilon}_0}{\dot{\varepsilon}}\right), \qquad [10]$$

where G is the shear modulus, k_B the Boltzmann constant, T temperature, b Burgers vector, r precipitate radius, $\dot{\varepsilon}$ the applied strain rate, and $\dot{\varepsilon}_0$ the reference strain rate of a particle-free material at the same stress. The applied strain rate is $\dot{\varepsilon} = 8 * 10^{-5}$ 1/s (equivalent to 0.005 1/min). The choice of $\dot{\varepsilon}_0$ is not critical, as the ratio $\dot{\varepsilon}_0/\dot{\varepsilon}$ enters the equation logarithmically. We will choose $\dot{\varepsilon}_0 = 10^{-2}$ 1/s.[33] The threshold stress for dislocation detachment τ_d is given by[15]

$$\frac{\tau_d}{\tau_o} = \sqrt{1 - k^2}, \qquad [11]$$

where τ_o is the Orowan stress. As mentioned above, the Orowan stress is used for reference as the ideal maximum strength where the precipitates are hard obstacles, and dislocations can propagate only by dislocation looping around the precipitates. The ratio τ/τ_o informs what fraction of that idealized situation can be sustained at high temperatures when thermally activated processes become significant, and what precipitate sizes will result

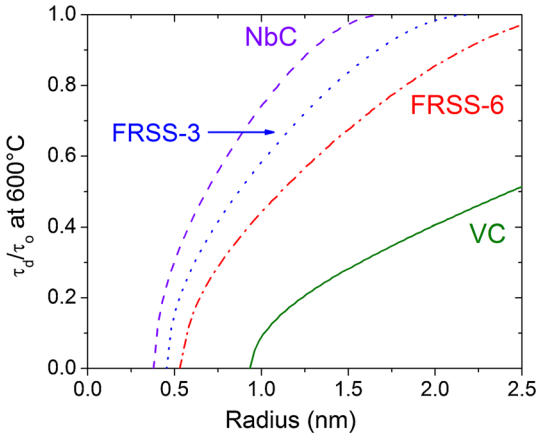

Fig. 9—Ratio of τ_d/τ_o (Eq. [11], Ref. [15]) at 873 K (600 °C) *vs* precipitate radius for VC (green solid line), NbC (purple dashed line), and mixed-composition precipitates with the compositions measured by atom probe tomography in FRSS-3 (blue dotted line) and FRSS-6 (red dash-dotted line) (Color figure online).

in a best-case scenario. Smaller values of k imply stronger attraction between the dislocation and the precipitate and hence a larger detachment stress, and hence a higher fraction of Orowan stress retained. Figure 9 shows k *vs* precipitate radius for pure VC, NbC, and the mixed-composition precipitates found in FRSS-3 and -6. Note that $\tau_d/\tau_o = 1$, or $k = 0$, is the limit at which the entire dislocation energy (Eq. [6]) is completely relaxed, representing maximum elastic interaction and maximum detachment stress.

Figure 9 shows that precipitates with larger misfit strains (NbC) attain higher detachment stresses and at smaller radii compared with VC and mixed-composition carbides. Furthermore, the graph shows that significant fractions of the Orowan strength can be retained at high temperatures both by NbC and VC-type precipitates in the size range observed in our investigation by APT (1 to 2.5 nm radius). Effectively, the strength gained from a finely dispersed network of small, slowly coarsening precipitates can be the primary strengthening mechanism at high temperatures when detachment stress due to attractive interaction between dislocations and precipitates is considered.

IV. CONCLUSIONS

In this paper, we outline a strategy to design lightly alloyed fire-resistant steels with the goal of retaining two-thirds of the room-temperature yield strength at 873 K (600 °C). This was accomplished through the incorporation of Nb and V to form semi-coherent, thermally stable MX-type precipitates with the B1 structure for strengthening at elevated temperatures, and including alloying elements such as Mo to slow diffusion. Based on phase diagrams obtained from thermodynamic modeling, we obtained three prototype steels and characterized them in terms of microstructure and mechanical properties at room and elevated temperature. The major findings are summarized as follows:

(a) Two types of precipitates, MX and M_2X, were observed by APT after exposure to 873 K (600 °C). Thermodynamic modeling showed that the MX phase fraction increases with V concentration, while M_2X phase fraction increases with Cr concentration.
(b) APT analysis demonstrates the presence of nanometer-sized MX or M_2X precipitates in FRSS-3 and -6 after exposure to 873 K (600 °C).
(c) MX or M_2X precipitates in FRSS-3 and -6 remain in the nanometer-sized regime after 27-hour exposure to 873 K (600 °C), demonstrating thermal stability of the precipitate microstructure.
(d) The fraction of yield strength retained at 873 K (600 °C) (yield strength ratio) increases with increasing V content and equilibrium MX volume fraction. FRSS-5 and -6 contain the highest V content (0.18 to 0.19 wt pct), and FRSS-6 achieves the highest yield strength ratios after 2 hours at 873 K (600 °C) of 0.69 and 0.83 in tension and compression, respectively, surpassing the proposed fire standard for structural steels.
(e) An analysis of dislocation–precipitate interactions in terms of a detachment stress shows that this model can explain the effectiveness of nanometer-sized precipitates in maintaining strength at high temperatures even when thermally activated processes become significant in limiting tensile strength.

ACKNOWLEDGMENTS

The authors would like to acknowledge the NSF CMMI Division [Grant Numbers NSF-CMMI-1130000 and CMMI-1462850] for providing funding for this research and Nucor for supplying one of the alloys *gratis* used in this research. This work made use of the MatCI Facility which receives support from the MRSEC Program (NSF DMR-1720139) of the Materials Research Center at Northwestern University. APT was performed at the Northwestern University Center for Atom Probe Tomography (NUCAPT). The local-electrode atom probe tomograph at NUCAPT was acquired and upgraded with equipment grants from the MRI Program of the National Science Foundation (NSF DMR-0420532) and the DURIP Program of the Office of Naval Research (N00014-0400798, N00014-0610539, N00014-0910781, N00014-1712870). NUCAPT received support from the MRSEC Program (NSF DMR-1720139) at the Materials Research Center, the SHyNE Resource (NSF ECCS-1542205), and the Institute for Sustainability and Energy at Northwestern (ISEN).

REFERENCES

1. T.J. MacGinley: *Steel Structures: Practical Design Studies*, 2nd ed., CRC Press, Boca Raton, 1998.
2. Y. Mizutani, K. Ishibashi, K. Yoshii, Y. Watanabe, R. Chijhwa, and Y. Yoshida: *Shinnittetsu Giho*, July 2004, pp. 38–44.
3. *Standard Test Methods for Fire Tests of Building Construction and Materials*, ASTM International, 2000.
4. D.B. Moore and T. Lennon: *Prog. Struct. Eng. Mater.*, 1997, vol. 1, pp. 4–9.
5. M.G. Goode: Fire Protection of Structural Steel in High-Rise Buildings, NIST, 2004, p. 88.
6. *AISC Specification for Structural Steel Buildings*, American Institute of Steel Construction, 2010, p. 610.
7. W. Sha, F.S. Kelly, and Z.X. Guo: *J. Mater. Eng. Perform.*, 1999, vol. 8, pp. 606–12.
8. Y.D. Morozov, O.N. Chevskaya, G.A. Filippov, and A.N. Muratov: *Metallurgist*, 2007, vol. 51, pp. 356–66.
9. W.-B. Lee, S.-G. Hong, C.-G. Park, and S.-H. Park: *Metall. Mater. Trans. A*, 2002, vol. 33A, pp. 1689–98.
10. M. Assefpour-Dezfuly, B.A. Hugaas, and A. Brownrigg: *Mater. Sci. Technol.*, 1990, vol. 6, pp. 1210–14.
11. R. Wan, F. Sun, L. Zhang, and A. Shan: *Mater. Des.*, 2012, vol. 36, pp. 227–32.
12. Z.-Y. Zhang, Q.-L. Yong, X.-J. Sun, Z.-D. Li, J.-Y. Kang, and G.-D. Wang: *J. Iron Steel Res. Int.*, 2015, vol. 22, pp. 337–43.
13. E. Arzt and D. Wilkinson: *Acta Metall.*, 1986, vol. 34, pp. 1893–98.
14. J. Rösler and E. Arzt: *Acta Metall.*, 1988, vol. 36, pp. 1043–51.
15. E. Arzt and J. Rösler: *Acta Metall.*, 1988, vol. 36, pp. 1053–60.
16. J. Rösler and E. Arzt: *Acta Metall. Mater.*, 1990, vol. 38, pp. 671–83.
17. C. Wagner: *Z. Elektrochem.*, 1961, vol. 65, pp. 581–91.
18. I. Lifshitz and V. Slyozov: *J. Phys. Chem. Solids*, 1961, vol. 19, pp. 35–50.
19. C. Enloe, K. Findley, C. Parish, M. Miller, B. De Cooman, and J. Speer: *Scripta Mater.*, 2013, vol. 68, pp. 55–58.
20. P. Maugis and M. Gouné: *Acta Mater.*, 2005, vol. 53, pp. 3359–67.
21. M. Perez, E. Courtois, D. Acevedo, T. Epicier, and P. Maugis: *Philos. Mag. Lett.*, 2007, vol. 87, pp. 645–56.
22. H.-J. Kestenbach and E.V. Morales: *Acta Micro*, 1998, vol. 7, pp. 22–33.
23. Z.-G. Yang and M. Enomoto: *Mater. Sci. Eng. A*, 2002, vol. 332, pp. 184–92.
24. E.K. Storms and C.P. Kempter: *J. Chem. Phys.*, 1965, vol. 42, p. 2043.
25. E.K. Storms and N.H. Krikorian: *J. Chem. Phys.*, 1959, vol. 63, pp. 1747–49.
26. C.P. Kempter and E.K. Storms: *J. Less Common Met.*, 1967, vol. 13, pp. 443–47.
27. K. Miyata, T. Kushida, T. Omura, and Y. Komizo: *Metall. Mater. Trans. A*, 2003, vol. 34A, pp. 1565–73.
28. D.J. Larson, T.J. Prosa, R.M. Ulfig, B.P. Geiser, and T.F. Kelly: *Local Electrode Atom Probe Tomography: A User's Guide*, Springer, New York, 2013.
29. *Standard Test Methods of Compression Testing of Metallic Materials at Room Temperature*, ASTM International, 2009.
30. *Standard Practice for Compression Tests of Metallic Materials at Elevated Temperatures with Conventional or Rapid Heating Rates and Strain Rates*, ASTM International, 2000.
31. *Standard Test Methods for Elevated Temperature Tension Tests of Metallic Materials*, ASTM International, 2009.
32. M. Boccalini Jr. and A. Sinatora: *6th International Tooling Conference Proceedings*, 2002, pp. 509–24.
33. H.J. Frost and M.F. Ashby: *Deformation-Mechanism Maps: The Plasticity and Creep of Metals and Ceramics*, Pergamon Press, Oxford, 1982.